Preparation of LiO・2SiO Ceramics with Oriented Microstructures by Unidirectional Solidification of Their Melts

AUTHOR(S):

Kokubo, Tadashi; Arioka, Masayuki; Tashiro, Megumi

CITATION:

Kokubo, Tadashi ...[et al]. Preparation of LiO・2SiO Ceramics with Oriented Microstructures by Unidirectional Solidification of Their Melts. Bulletin of the Institute for Chemical Research, Kyoto University 1980, 57(5-6): 355-375

ISSUE DATE:

1980-01-31

URL:

http://hdl.handle.net/2433/76849

Bull. Inst. Chem. Res., Kyoto Univ., Vol. 57, Nos. 5~6, 1979

Preparation of $Li_2O \cdot 2SiO_2$ Ceramics with Oriented Microstructures by Unidirectional Solidification of Their Melts

Tadashi KOKUBO, Masayuki ARIOKA, and Megumi TASHIRO*

Received September 20, 1979

The results of a series of the present authors' investigation on unidirectional solidification of the melts with the compositions of $Li_2O \cdot 2SiO_2$ and its neighbors are described. The conditions for obtaining dense $Li_2O \cdot 2SiO_2$ polycrystalline ceramics with oriented microstructures, and some physical properties, such as thermal expansion, sound propagation rate and compressive strength of the resultant ceramics were investigated.

KEY WORDS: Unidirectional solidification/ $Li_2O \cdot 2SiO_2$ ceramics/ Preferred orientation/ Porosity of ingot/ Thermal expansion/ Compressive strength/

I. INTRODUCTION

Most of the conventional ceramics are composed of randomly distributed crystalline phases and show isotropic physical properties. In the last decade special attention has been focused on producing ceramics with oriented microstructure which show anisotropic properties and have potential for unique structural or electrical applications.

Typical methods employed hitherto for producing such ceramics are; a) to press plate-like crystalline powders uniaxially and then to sinter,[1-6] b) to crystallize glasses unidirectionally by special heat treatments,[7-16] and c) to solidify melts unidirectionally.[17-35] However, the first method a) is applicable only to the system for which plate-like crystalline powders can be easily obtained as starting materials, and the method b) is applicable only to limited compositions the melt of which could be supercooled into a glassy state. The method c) has hitherto been used most frequently for producing oxide ceramics with aligned composite microstructure, but was applied only to the melts of the eutectic compositions.

The present authors have attempted to produce single phase-ceramics with oriented microstructure by unidirectional solidification of the melts which solidify congruently. In the present article, the results of a series of our investigation[36-40] on unidirectional solidification of the melts with compositions of $Li_2O \cdot 2SiO_2$ and its neighbors are described. The $Li_2O \cdot 2SiO_2$ composition was chosen because it melts congruently at fairly low temperature (~1034°C,[41] see APPENDIX) and physical properties of its melt and crystal are both known in detail. The main objectives of the present investigation are to find out the conditions for producing dense $Li_2O \cdot 2SiO_2$ polycystalline ceramics with oriented microstructure and to analyze the parameters controlling

* 小久保 正, 有岡 雅行, 田代 仁: Laboratory of Ceramic Chemistry, Institute for Chemical Research, Kyoto University, Uji, Kyoto.

the resultant structures. Since the $Li_2O{\cdot}2SiO_2$ melt is viscous even at high temperatures, the results of this investigation may form a general guide to unidirectional solidification of viscous silicate melts.

II. EXPERIMENTAL PROCEDURE

1. Unidirectional Solidification

About 160 g of batch mixtures with the compositions of $Li_2O{\cdot}2SiO_2$ and 100 $(Li_2O{\cdot}2SiO_2)3R_mO_n$ in mole ratio, where R_mO_n is Na_2O, MgO, B_2O_3, Al_2O_3, SiO_2, or P_2O_5, were prepared from the reagent grade chemicals of Li_2CO_3, Na_2CO_3, MgO, B_2O_3, Al_2O_3, SiO_2, and P_2O_5. They were melted in a Pt10%Rh crucible at 1400°C for 6 h in a SiC electric furnace. The melts were poured into a clay crucible 45 mm in inner diameter, 55 mm in depth and 3 mm in thickness. In some cases, the inner surface of the bottom of the clay crucible had been previously covered with a platinum foil, sintered $Li_2O{\cdot}2SiO_2$ ceramic plate about 2 mm thick or $Li_2O{\cdot}2SiO_2$ glass-ceramic layer about 2 mm thick. The sintered $Li_2O{\cdot}2SiO_2$ ceramic plate was prepared by sintering a compressed mass of $Li_2O{\cdot}2SiO_2$ crystal powders at 900°C for 6 h. The $Li_2O{\cdot}2SiO_2$ glass-ceramic layer was prepared by heating a $Li_2O{\cdot}2SiO_2$ glassy layer previously formed on the inner surface of the bottom of the clay crucible to 900°C at a rate of 300°C/h and keeping it at that temperature for 3 h.

The clay crucible empty of the melt was first placed in a temperature gradient furnace schematically shown in Fig. 1. The temperature of its top was held at 1200°C with SiC heating elements. Its bottom was cooled by using a water-cooled copper jacket. When the melt was poured into the clay curcible, it solidified immediately up to the height of 10 mm from its bottom. Since many gas bubbles were formed in the remaining melt, the temperature at the top of the crucible was maintained at 1200°C further for 10 h to refine the melt. Its temperature was then lowered at a constant rate of 5, 10, 25, 50, or 100°C/h to solidify the melt upward unidirectionally.

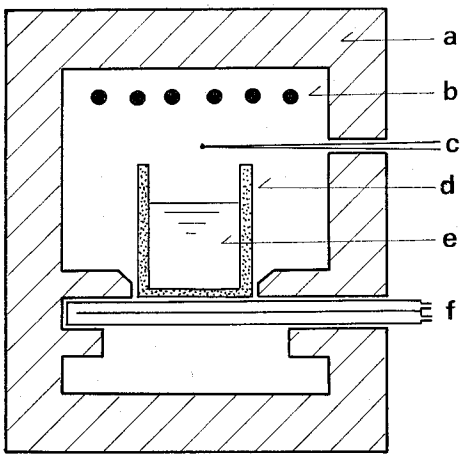

Fig. 1. Temperature gradient furnace used for unidirectional solidification of the $Li_2O{\cdot}2SiO_2$ and $100(Li_2O{\cdot}2SiO_2)3R_mO_n$ melts.
a; Refractory. b; SiC heating element. C; Thermocouple.
d; Clay crucible. e; Melt. f; Water-cooled copper jacket.

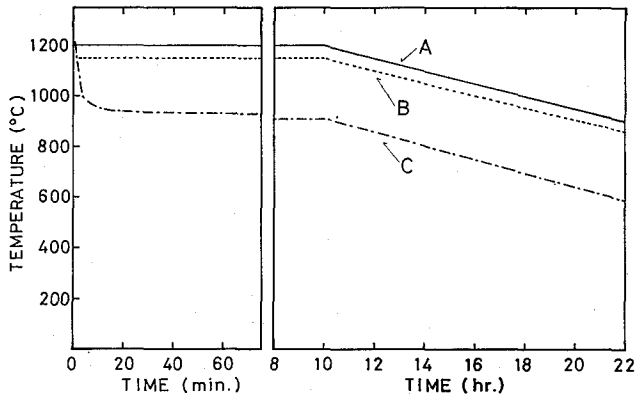

Fig. 2. Temperature changes at the top of the crucible (A), the upper surface of the melt (B) and the inner surface of the bottom of the crucible (C) during solidification process in which the temperature at the top of the crucible was first maintained at 1200°C for 10 h and then lowered at a rate of 25°C/h.

The curve A in Fig. 2 shows the change in temperature of the top of the crucible with time, when its temperature was lowered at a rate of 25°C/h. The curves B and C in Fig. 2 are for those of the upper surface of the melt and the inner surface of the bottom of the crucible, respectively, in the same run. The temperatures of these two surfaces were measured by Pt-Pt13Rh thermocouples inserted through the crucible wall from the outside to the respective surfaces. Figure 2 indicates that the temperature difference, B—C, between the surface of the melt and the bottom of the crucible was maintained at about 220°C throughout the cooling process. The temperature gradient in the specimen was obtained by dividing the temperature difference (B—C) by the height of the specimen, 27 mm; *i.e.* the distance from the upper surface of the melt to the bottom of the crucible. Its value was about 80°C/cm. In the other runs, in which the other cooling rates were used, the temperature gradients in the specimens were found almost the same.

The solidification rate of the melts in the region 10 mm or more above the bottom of the crucible, obtained by dividing the thermal gradient by the cooling rates, were 0.7, 1.3, 3.3, 6.7, and 13 mm/h for the cooling rates to 5, 10, 25, 50, and 100°C/h, respectively.

2. Analysis of Microstructure

2.1. X-Ray Diffraction

Rectangular pieces, approximately $5 \times 5 \times 3$ mm, were cut out from the ingots at the distance of 17–20 mm from their bottoms, powdered and subjected to X-ray diffraction analyses to identify the crystal phases precipitated and to determine contents of glassy phase in the specimens. The contents of the glassy phases were determined by Ohlberg's method[42]; *i.e.* the noncrystalline scattering intensities of the powdered specimens were compared with those of mechanical mixtures of $Li_2O \cdot 2SiO_2$ glass and $Li_2O \cdot 2SiO_2$ crystal powders in various weight ratios at the diffraction angles of $2\theta =$ 19.6°, 22.5°, and 27.6°. The glass contents determined at these three angles for each specimen were averaged and used for discussion.

Transverse sections of the ingots at the distance of 15 mm from their bottoms were subjected to X-ray diffraction analyses to determine degree of the preferred orientation of the $Li_2O{\cdot}2SiO_2$ crystals. The degree of the orientation $f(00\,l)$ was expressed by the relation used by Lotgering[43]:

$$f(00\,l)=\frac{P-P_0}{1-P_0} \tag{1}$$

$$P=\frac{\sum I(00\,l)}{\sum I(hk\,l)} \tag{2}$$

where $\sum I(00l)$ and $\sum I(hkl)$ are the sum of the intensities of the $(00l)$ reflections and that of all the (hkl) reflections in the range of the diffraction angle 2θ from 20° to 50°, and P and P_0 are the values given by the Eq. (2) for the transverse section of the specimen and its powder (non-oriented specimen), respectively. For the specimen in which the $\langle 001\rangle$ direction of the crystals is ideally oriented perpendicularly to its transverse section, $f(00l)=1$, whereas for that with non-oriented structure, $f(00l)=0$.

2.2. Optical and Electron Microscopies

The ingots were transversely sectioned at various distances from their bottoms, polished and observed under a polarizing or metallurgical microscope to determine the diameter of the crystals and pore distribution. The mean diameters (D) of the $Li_2O{\cdot}2SiO_2$ columnar crystals were determined from the number (N) of the crystals in the area (S) of 2×3 mm, in the transverse sections cut out from the ingots at the distance of 15 mm from their bottoms, by using the equation $\pi(D/2)^2=S/N$.

Some of the sections were etched with 1%HF aqueous solution and observed with a scanning electron microscope (Hitachi-Akashi, Model MSM-11) to determine pore distribution in more detail.

3. Measurement of Porosity

Cubic pieces, $10\times10\times10$ mm, cut out from the ingots at the distance of 12–22 mm from their bottoms, were subjected to measurements of their bulk densities using Archimedean technique. The true densities of the specimens were measured by a pycnometer method after they were powdered. The reagent grade chemical of toluene was used as the immersion liquid in the measurements. The true porosities of the specimens were determined from the bulk and true densities.

4. Massspecroscopy

To investigate the origin of the bubbles formed during the solidification of the melts, the clay crucible containing the $Li_2O{\cdot}2SiO_2$ melt was taken out from the furnace in the middle of the solidification, and one of the bubbles remaining in the melt was spooned up together with the surrounding melt with a platinum spatula and allowed to cool in air. A piece of glass containing the bubble was placed in a sample chamber of a quadrupole massspectrometer (Finnigan, Model RGA-400) and broken mechanically into pieces to release the gas from the bubble inside of the massspectrometer.

5. Infrared Spectroscopy

The $Li_2O{\cdot}2SiO_2$ melt, after refined for 10 h in the clay crucible, in the beginning of the unidirectional solidification process, was taken out from the furnace together

with the crucible and allowed to cool in air. A portion of the resulting glass adjacent to the previously crystallized part was sliced, polished to the thickness of 1.4 mm and subjected to infrared spectroscopy for determination of its H_2O-content.

On the other hand, the $Li_2O \cdot 2SiO_2$ melt, after refined for 10 h and unidirectionally solidified at a rate of 1.3 mm/h, was remelted in a Pt10%Rh crucible in a N_2 atmosphere for a short time and poured onto a steel plate to be formed into a plate. The resulting glass, after polished to the thickness of 1.4 mm, was subjected to infrared spectroscopy.

6. Measurement of Thermal Expansion

Rectangular pieces, $5 \times 5 \times 15$ mm, with the long axis parallel or perpendicular to the bottom of the crucible were cut out from the ingots at the distance of 10–25 mm from their bottoms. Their thermal expansions along the long axes were measured with an automatic recording dilatometer (Shimazu, Model TMA-30) at a heating rate of 5°C/min.

For reference, the thermal expansions of the $Li_2O \cdot 2SiO_2$ crystal, which was reported of pseudo-orthorhombic system, along its crystallographic axes were determined by high temperature X-ray diffraction technique in the temperature range of 20–900°C. The specimen used was the powdered $Li_2O \cdot 2SiO_2$ crystals obtained by crystallization of the $Li_2O \cdot 2SiO_2$ glass powders.

7. Measurement of Sound Velocity

Cubic pieces, $10 \times 10 \times 10$ mm, were cut out from the ingots at the distance of 15–25 mm from their bottoms. Propagation rates of a 12MHz longitudinal sound wave in the specimens were measured in the directions parallel and perpendicular to the bottoms of the ingots by pulse transmission method.[45]

8. Measurement of Compressive Strength

Cubic pieces, $7 \times 7 \times 7$ mm, were cut out from the ingots at the distance of 15–25 mm from their bottoms. The compressive strengths of the specimens were determined in the directions parallel and perpendicular to the bottoms of the ingots. The loading rate used was 7 Kg/s. Ten measurements were made on each of the ingots.

III. RESULTS AND DISCUSSION

All the melts were transformed, by the unidirectional solidification, into the white dense ingots composed of many columnar crystals, as shown in Fig. 3. The X-ray diffraction analyses indicated that for all the ingots the main crystalline phase was the $Li_2O \cdot 2SiO_2$ crystal and a small amount of glassy phase was in coexistence. In the $100(Li_2O \cdot 2SiO_2)3R_mO_n$ ingots, the other kinds of crystalline phases were also detected although in a small amount. The crystalline phases detected and the content of the glassy phase estimated are listed in Table I.

1. Orientation of the Crystals

When the $Li_2O \cdot 2SiO_2$ melt was unidirectionally solidified in the as-prepared clay crucible, which has a fresh bottom surface, at a rate of 3.3 mm/h, the $Li_2O \cdot 2SiO_2$ crystals nucleated only from a few points on the bottom surface of the crucible and grew

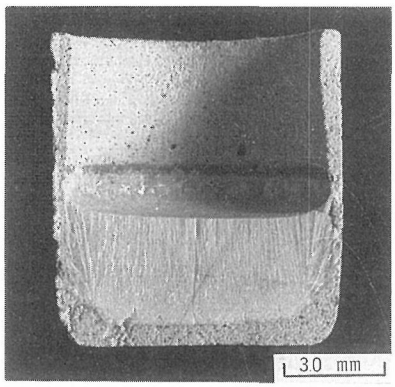

Fig. 3. A longitudinal section of the $Li_2O \cdot 2SiO_2$ ingot solidified at a rate of 3.3 mm/h.

Table I. Composition, Solidification Condition and Microstructure of Ingots

Specimen	Composition (in mole)	Solidification rate (mm/h)	Crystal phase*	Diameter of L crystal (μm)	Glass content (wt%)	True porosity (%)
L2S-1	$Li_2O \cdot 2SiO_2$	13	L	340	3	11.3
L2S-2	$Li_2O \cdot 2SiO_2$	6.7	L	420	3	10.2
L2S-3	$Li_2O \cdot 2SiO_2$	3.3	L	460	3	5.5
L2S-4	$Li_2O \cdot 2SiO_2$	1.3	L	540	2	3.4
L2S-5	$Li_2O \cdot 2SiO_2$	0.7	L	580	2	3.0
L2S-B	$Li_2O \cdot 2SiO_2 + 0.03B_2O_3$	1.3	L, Q, C	170	5	1.7
L2S-Na	$Li_2O \cdot 2SiO_2 + 0.03Na_2O$	1.3	L, Q	240	7	1.1
L2S-Mg	$Li_2O \cdot 2SiO_2 + 0.03MgO$	1.3	L, C, Q, F	210	3	3.2
L2S-Al	$Li_2O \cdot 2SiO_2 + 0.03Al_2O_3$	1.3	L, S, C	220	1>	9.1
L2S-Si	$Li_2O \cdot 2SiO_2 + 0.03SiO_2$	1.3	L, C	410	4	2.7
L2S-P	$Li_2O \cdot 2SiO_2 + 0.03P_2O_5$	1.3	L, C, Q, P	310	1>	7.6

* L, $Li_2O \cdot 2SiO_2$ crystal; Q, α-Quartz; C, α-Cristobalite; F, Forsterite; S, β-Spodumene; P, Li_3PO_4 crystal.

radially. However, when the same melt was solidified in the clay crucibles, the bottoms of which had been previously covered with the platinum foil, the sintered $Li_2O \cdot 2SiO_2$ ceramic plate or the $Li_2O \cdot 2SiO_2$ glass-ceramic layer, the $Li_2O \cdot 2SiO_2$ crystals nucleated from numerous points on the surface of these materials and grew upwards and almost in parallel with each other. The most highly oriented columnar structure was obtained when the crucible, the bottom of which had been covered with the $Li_2O \cdot 2SiO_2$ glass-ceramic layer, was used.

The X-ray diffraction patterns of the transverse sections of these ingots are shown in Fig. 4, in which that of the powdered $Li_2O \cdot 2SiO_2$ crystals is also shown for comparison. Factors of the orientation degree of the $Li_2O \cdot 2SiO_2$ crystals, $f(00l)$ obtained from these X-ray patterns are shown in Table II. It can be seen from Fig. 4 and Table II that the ingot solidified in the as-prepared clay crucible shows no crystallographic orientation, whereas the ingots solidified in the other clay crucibles, the bottom surfaces of which were covered with various materials as described above, show high

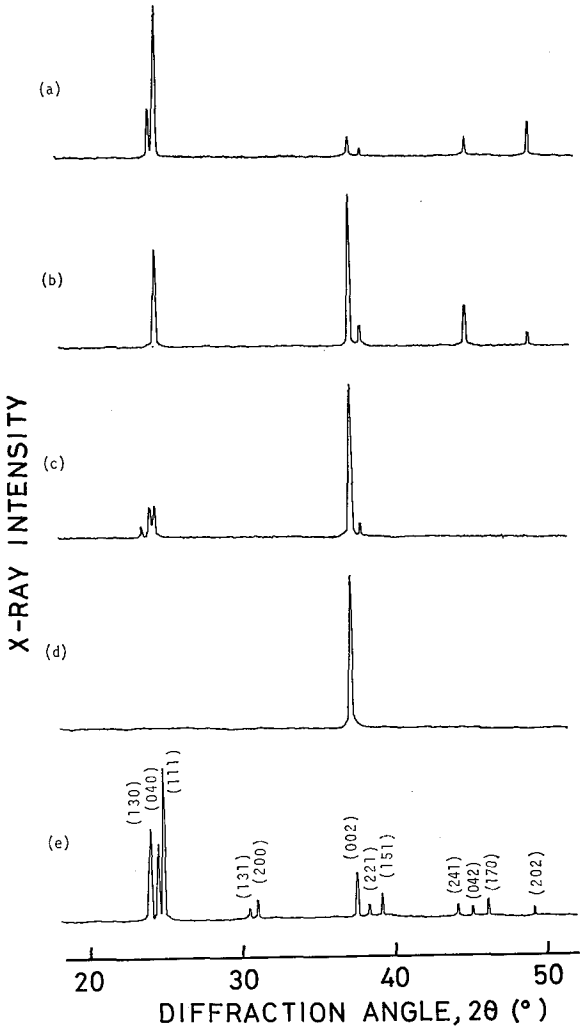

Fig. 4. The X-ray diffraction patterns taken of the transverse sections of the $Li_2O \cdot 2SiO_2$ ingots solidified in various clay crucibles the bottom surface of which had been fresh (a), or covered with a platinum foil (b), a sintered $Li_2O \cdot 2SiO_2$ ceramic plate (c) or a $Li_2O \cdot 2SiO_2$ glass-ceramic layer (d). The pattern (e) is that of powdered $Li_2O \cdot 2SiO_2$ crystals.

Table II. Degree of Orientation $f(00l)$ of the $Li_2O \cdot 2SiO_2$ Crystals Solidified in Various Clay Crucibles

Bottom of crucible	$f(00l)$
Covered with nothing	0.00
Covered with a platinum foil	0.43
Covered with a sintered $Li_2O \cdot 2SiO_2$ ceramic plate	0.61
Covered with a $Li_2O \cdot 2SiO_2$ glass-ceramic layer	1.00

degrees of orientation. The ⟨001⟩ direction of the oriented $Li_2O \cdot 2SiO_2$ crystals in the ingots was in parallel with the elongation direction of the columnar crystals. The degree of their orientation depended on the kind of materials applied on the bottom surface of the crucible: The sintered $Li_2O \cdot 2SiO_2$ ceramics plate gave a fairly high degree of orientation to the precipitated crystals, 0.61, although the degree of orientation of the ceramics plate itself was extraordinarily low, *i.e.* −0.09. The $Li_2O \cdot 2SiO_2$ glass-ceramic layer with the high degree of orientation, 0.88, gave almost perfect orientation to the precipitated crystals.

The fact that the ingot with a fairly high degree of orientation could be obtained even when the orientation degree of the seed crystal layer was extraordinarily low indicates that the high crystallographic orientation of the seed crystal layer is not a prerequisite for obtaining the ingots with highly oriented microstructure. Its cause may be interpreted as follows: When the nuclei are densely formed, crystals originating from the nuclei soon mutually impinge and only the crystals whose elongation direction are perpendicular to the bottom of the crucible survive, giving highly oriented columnar microstructure.

The melts with other compositions (Table I) also gave ingots with almost perfectly oriented microstructure, when the $Li_2O \cdot 2SiO_2$ glass-ceramic layer was used as the seed crystal layer. The following results are all concerned with the ingots the microstructures of which were highly oriented by using the glass-ceramic layer as the seeds.

2. Diameter of the Crystals

An optical micrograph of a transverse section of the $Li_2O \cdot 2SiO_2$ ingot solidified at a rate of 1.3 mm/h is shown in Fig. 5. The cross-section of the $Li_2O \cdot 2SiO_2$ columnar crystals in all the ingots was generally angular. For calculation of their diameter, however, it was assumed to be circular. The mean diameters of the $Li_2O \cdot 2SiO_2$ columnar crystals in the $Li_2O \cdot 2SiO_2$ ingots solidified at various rates and in the $100(Li_2O \cdot 2SiO_2)3R_mO_n$ ingots solidified all at a rate of 1.3 mm/h are shown in Table I.

The mean diameters of the columnar crystals ranged from 170 to 580 μm, which were much larger than that (about 10 μm) of the $Li_2O \cdot 2SiO_2$ crystals in the seed crystal (glass-ceramic) layer. Table I indicates that the mean diameter of the columnar

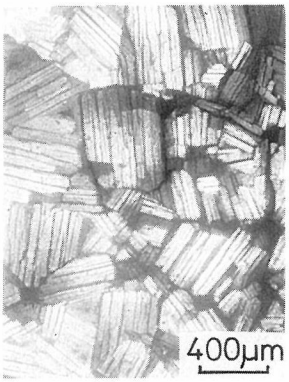

Fig. 5. Optical micrograph of a transverse section of the $Li_2O \cdot 2SiO_2$ ingot solidified at a rate of 1.3 mm/h.

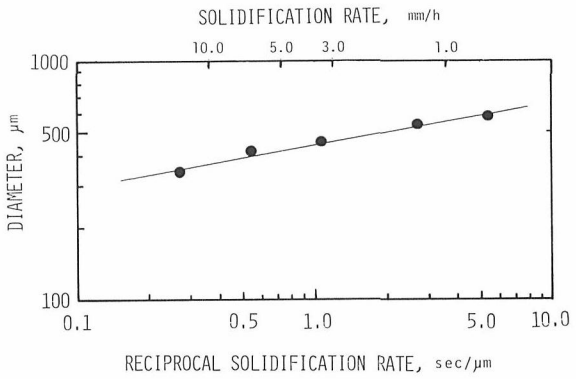

Fig. 6. Mean diameter of the $Li_2O \cdot 2SiO_2$ columnar crystals in the ingots as a function of their solidification rates.

crystals decreases with increasing solidification rate and also by addition of the third components. Relation between the mean diameter (D) of the columnar crystals in the $Li_2O \cdot 2SiO_2$ ingots and their solidification rate (R) is shown in Fig. 6. It is represented by the equation $D \propto R^{-1/6}$.

3. Porosity of the Ingot

True porosities of the $Li_2O \cdot 2SiO_2$ and $100(Li_2O \cdot 2SiO_2)3R_mO_n$ ingots are shown in Table I. They ranged from 1.1 to 11.3%. Table I indicates that the porosity of the $Li_2O \cdot 2SiO_2$ ingots decreases markedly with decreasing solidification rate down to about 4%, but below this value its decrease becomes more sluggish and finally stops.

In the $Li_2O \cdot 2SiO_2$ ingots solidified at rates higher than 3.3 mm/h a number of cylindrical pores, as shown in Fig. 7(a), were observed indiscriminately, while in those solidified at rates lower than 1.3 mm/h no cylindrical pores were observed, but a few microcracks at crystal boundaries, as shown in Fig. 7(b). These results suggest that the porosities higher than about 5% of the ingots solidified at rates higher than 3.3 mm/h are attributed to the existence of the cylindrical pores while those lower than about 4% of the ingots solidified at rates lower than 1.3 mm/h are attributed to the existence of the microcracks.

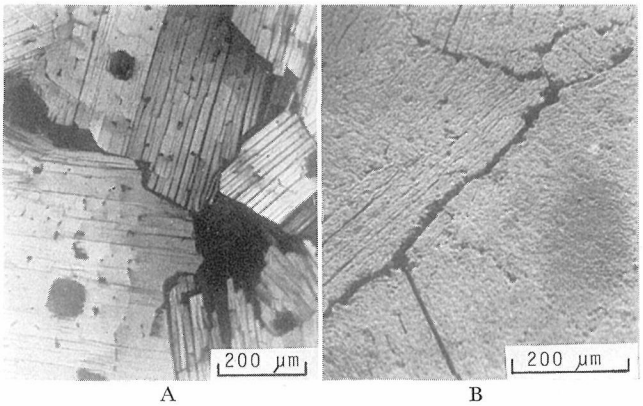

A B

Fig. 7. Micrographs of transverse sections of the $Li_2O \cdot 2SiO_2$ ingots solidified at rates of 3.3 mm/h (A; optical) and 1.3 mm/h (B; SEM), respectively.

Table I also indicates that the porosity of the $Li_2O \cdot 2SiO_2$ ingots is markedly increased by the addition of the Al_2O_3 or P_2O_5 while that is markedly decreased by the addition of the Na_2O or B_2O_3. In the $100(Li_2O \cdot 2SiO_2)3Al_2O_3$(or P_2O_5) ingots, having the porosity higher than 7% ,many cylindrical pores were observed, while in the $100(Li_2O \cdot 2SiO_2)3Na_2O$(or B_2O_3), having the porosity lower than 2%, no cylindrical pores but only few microcracks were observed.

4. Origin of the Cylindrical Pores

The infrared spectra of two kinds of the $Li_2O \cdot 2SiO_2$ glasses, one prepared by refining its melt in the clay crucible and allowing to cool in air, and another prepared by subjecting the above melt to unidirectional solidification and then remelting for a short time and pouring onto steel plate, are shown in Fig. 8. Their infrared absorptions at the wavelengths of 2.9, 3.5 and 4.2 μm are all attributed to the H_2O dissolved in the glasses.[46] The contents of the H_2O estimated from the intensities of the spectra by using the values of the extinction coefficients reported for the $Li_2O \cdot 4SiO_2$ glass by Scholze[47] were 0.025 and 0.003 mol/l for the respective glasses above described. This result suggests that the solubility of the H_2O in the initial melt (or glass) is lowered drastically by its solidification. This suggests further that the H_2O initially contained in the $Li_2O \cdot 2SiO_2$ melt will be expelled and accumulate in the melt adjacent to the ascending crystal surface in the process of its unidirectional solidification, as schematically shown in Fig. 9.

The H_2O concentration C_{gx} in the melt at the distance of x from the crystal surface at the time t after the beginning of solidification is represented by:

$$D\frac{\partial^2 C_{gx}}{\partial x^2}+R\frac{\partial C_{gx}}{\partial x}=\frac{\partial C_{gx}}{\partial t} \tag{3}$$

where D is the diffusion coefficient of the H_2O in the melt and R is the solidification rate. Assuming that the H_2O solubility in the crystal is negligibly small, at $x=0$ for all t:

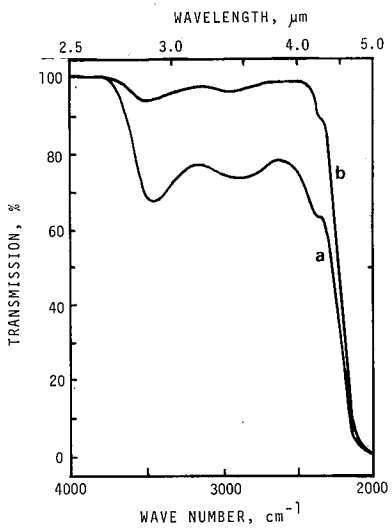

Fig. 8. Infrared spectra of the $Li_2O \cdot 2SiO_2$ glasses prepared from a melt before solidification (a) and from that remelted after solidification (b).

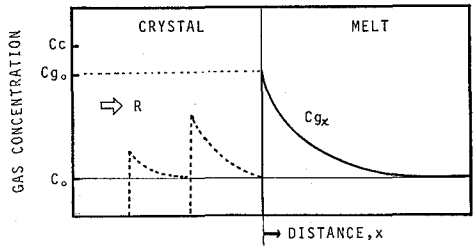

Fig. 9. Schematic representation of gas distribution in a solidifying melt.

$$RC_{go}+D\left(\frac{\partial C_{gx}}{x}\right)_{x=0}=0 \tag{4}$$

where C_{go} is the H_2O concentration at the crystal surface. At $x=\infty$ for all t:

$$C_{g\infty}=C_0 \tag{5}$$

where C_0 is the initial H_2O concentration in the melt. At $t=0$ for all x:

$$C_{gx}=C_0 \tag{6}$$

Under the boundary conditions (4) to (6), Eq. (3) can be solved:

$$\frac{C_{gx}}{C_0}=\frac{1}{2}\mathrm{erfc}\left[-\frac{x+Rt}{2\sqrt{Dt}}\right]+\frac{1}{2}\exp\left[-\frac{Rx}{D}\right]\mathrm{erfc}\left[\frac{x-Rt}{2\sqrt{Dt}}\right]+\frac{R\sqrt{t}}{\pi D}\exp\left[-\frac{Rx}{D}\right]\exp\left[\frac{(x-Rt)^2}{4Dt}\right]-\frac{R}{2D}(x-Rt)\exp\left[-\frac{Rx}{D}\right]\cdot\mathrm{erfc}\left[\frac{x-Rt}{2\sqrt{Dt}}\right] \tag{7}$$

At $x=0$:

$$\frac{C_{go}}{C_0}=\mathrm{erfc}\left[-\frac{R}{2}\sqrt{\frac{t}{D}}\right]+\frac{R\sqrt{t}}{\sqrt{\pi D}}\exp\left[-\frac{R^2t}{4D}\right]+\frac{R^2t}{2D}\mathrm{erfc}\left[\frac{R\sqrt{t}}{2\sqrt{D}}\right] \tag{8}$$

When $R\sqrt{t}/2\sqrt{D}\gg 1$:

$$C_{go}=C_0\left(\frac{R^2}{D}t+2\right) \tag{9}$$

Equation (9) indicates that the H_2O concentration in the melt adjacent to the crystal surface increases in proportion to the time elapsed and the square of the solidification rate, and in inverse proportion to the diffusion coefficient of the H_2O in the melt. In such a viscous melt as the $Li_2O \cdot 2SiO_2$ melt, where D is low, the H_2O will be accumulated very rapidly at the crystal-melt interface, especially in the case when the solidification rate is high, and, when the H_2O concentration exceeds its critical supersaturated value, the H_2O bubbles will be formed in the melt near the ascending crystal surface.

Actually many bubbles were observed in the $Li_2O \cdot 2SiO_2$ melt taken out of the furnace in the middle of the solidification progressing at a rate of 13 mm/h. The massspectroscopic analysis of these bubbles showed that they were mainly composed of H_2O as shown in Fig. 10.

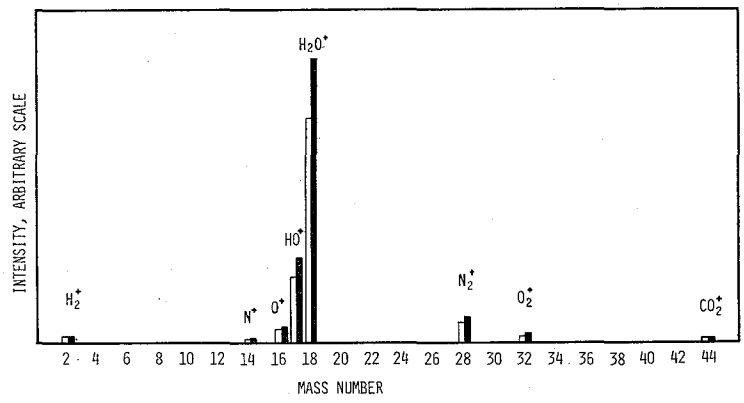

Fig. 10. Massspectroscopic analysis of the gas in a bubble caught by the $Li_2O{\cdot}2SiO_2$ glass: Massspectra of the gases in the massspectrometer before (□) and after (■) a piece of glass was broken.

The bubbles thus formed in the melt during the solidification will rise to the surface at the rate (V) given by:[48]

$$V=(1/12)d^2g\rho/\eta \tag{10}$$

where d, g, ρ and η are the diameter of the bubble, acceleration of gravity, and the density and viscosity of the melt. According to Eq. (10) the rising rate of the bubble decreases with decreasing diameter of the bubble. When the rising rate of the bubble is lower than the solidification rate of the melt, the bubble will be captured by the growing crystals and form a cylindrical pore in the ingot. The maximum diameter (d_{max}) of the bubble captured by the ingot solidifying at a given rate (R) is given by:

$$d_{max}=\sqrt{12\eta R/g\rho} \tag{11}$$

For the $Li_2O{\cdot}2SiO_2$ melt at the melting temperature, 1034°C, η and ρ are 350 poise and 2.17 g/cm^3,[49] respectively. Then the Eq. (11) is represented by the solid line shown in Fig. 11. The maximum diameters of the cylindrical pores determined experimentally on the transverse sections of the $Li_2O{\cdot}2SiO_2$ ingots solidified at rates of 3.3, 6.7, and 13 mm/h respectively are given by open circles in Fig. 11. The circles fall on the solid line representing Eq. (11).

No cylindrical pores were observed in the ingots solidified at rates lower than a limit. This suggests that in such ingots the H_2O concentration did not reached the critical supersaturated value at which the H_2O gas bubbles start to nucleate. These results emphasize the importance of lowering the solidification rate below a certain value for obtaining the cylindrical pore-free ingots especially from such viscous melts as the $Li_2O{\cdot}2SiO_2$ melt.

In the ingots solidified at a rate of 3.3 mm/h, the cylindrical pores were observed only in the region more than 2 mm apart from the line where the melt started to solidify after refined. This means that the bubbles formed 40 min after the solidification started. Diffusion coefficient of the H_2O in the $Li_2O{\cdot}2SiO_2$ melt at its melting point, 1034°C, is estimeted to be 1.6×10^{-6} cm^2/s from those for the Li_2O-SiO_2 melts reported by Scholze *et al.*[50] Inserting these values into the Eq. (9), one obtains the critical

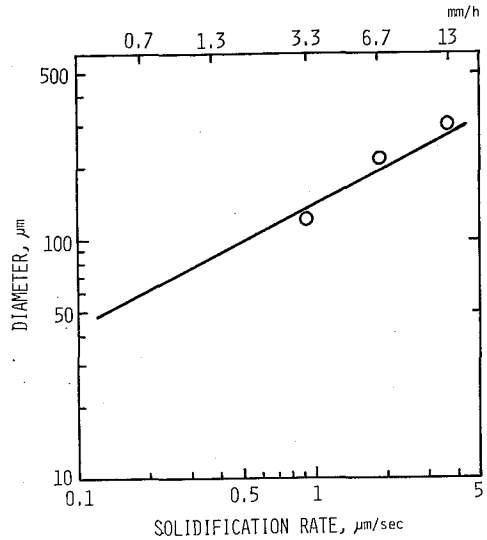

Fig. 11. Dependence of maximum diameter of cylindrical pores in the $Li_2O \cdot 2SiO_2$ ingots upon their solidification rates. Solid line; Eq. (11). Open circle; observed diameter.

supersaturated concentration (C_c) of the H_2O in the melt at its melting point, *i.e.* the H_2O concentration in the melt at which the H_2O gas bubbles start to form:

$$C_c = 15C_o \tag{12}$$

The initial concentration (C_o) of the H_2O in the melt is considered to be the saturated concentration, because the melt had been refined long before the solidification started. Equation (12) indicates that the critical supersaturated concentration is 15 times of the saturated concentration.

5. Origin of the Microcracks

The thermal expansion coefficients of the $Li_2O \cdot 2SiO_2$ single crystals, determined by the X-ray diffraction method, were 198, 90, and 142×10^{-7}/°C, in the directions of their *a*-, *b*-, and *c*-axes, respectively. As described previously, the constituent $Li_2O \cdot 2SiO_2$ crystals in all of the ingots were aligned with their *c*-axis parallel to the solidification direction of the ingots. Their *a*- and *b*-axes, however, were randomly distributed on planes perpendicular to the solidification direction of the ingots. Since there is much difference of thermal expansion coefficient between the *a*- and *b*-axes of the $Li_2O \cdot 2SiO_2$ crystals, the large thermal stresses must have been induced in the ingots when the ingots were cooled from their solidification temperature to room temperature. The micro-cracks observed at the crystal boundaries in the ingots, which were considered in the previous section to be the main source of the porosities lower than about 4%, were probably formed by such thermal stresses.

As shown in Table I, a fairly large amount of glassy phase is present in some of the $100(Li_2O \cdot 2SiO_2)3R_mO_n$ ingots, especially in the ingots with addition of the Na_2O or B_2O_3. If the glassy phase exists at the boundaries of the columnar $Li_2O \cdot 2SiO_2$ crystals the thermal stresses induced in the ingots by the large difference in thermal

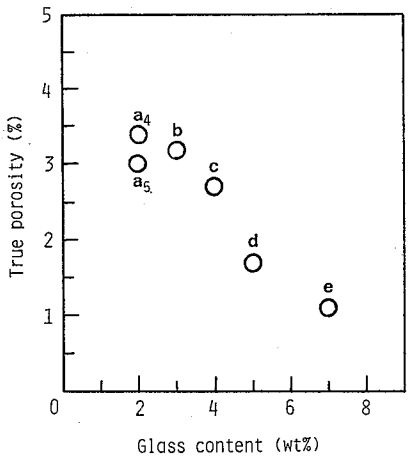

Fig. 12. True porosities of the cylindrical-pore-free ingots versus their glass contents.
a_4; L2S-4. a_5; L2S-5. b; L2S-Mg. c; L2S-Si. d; L2S-B. e; L2S-Na.

expansion coefficient between the *a*- and *b*- axes of the constituent $Li_2O{\cdot}2SiO_2$ crystals will be relieved by the viscous flow of the glassy phase and the formation of the microcracks will be suppressed. The relation between the porosities of the ingots containing no cylindrical pores and their glass content, which was derived from the data in Table I, is shown in Fig. 12, which shows that the porosity decreases with increasing the amount of the glassy phase in the ingots. This fact supports the assumption described above; *i.e.* the thermal stresses induced in the ingots will be relieved more easily by the viscous flow of the glassy phase as the amount of the glassy phase increases. It should be noted that the addition of a small amount of third components such as Na_2O and B_2O_3, which will form the glassy phase at the boundaries of the unidirectionally oriented columnar $Li_2O{\cdot}2SiO_2$ crystals, is effective in suppressing the formation of the microcracks.

The fact that the glassy phase is present at the boundaries of the unidirectionally aligned $Li_2O{\cdot}2SiO_2$ columnar crystals was verified, for example, the special shape of the thermal expansion curve, obtained in the direction perpendicular to the solidification direction of the $100(Li_2O{\cdot}2SiO_2)3B_2O_3$ ingot containing 5 wt% of glassy phase, as shown in Fig. 13; *i.e.* its curve had two bends similar to those as observed for glassy substances at their transition and softening temperatures, suggesting that the glassy phase existed in series with the crystal phase in the ingot. The thermal expansion curve of the same specimen in the direction parallel to its solidification direction, however, was almost linear up to 900°C.

6. Thermal Expansion of the Ingot

The thermal expansion curves obtained with the dilatometer of the $Li_2O{\cdot}2SiO_2$, $100(Li_2O{\cdot}2SiO_2)3Na_2O$ and $100(Li_2O{\cdot}2SiO_2){\cdot}3Al_2O_3$ ingots, all solidified at a rate of 1.3 mm/h, are shown in Fig. 14. For comparison, the thermal expansion curves of the $Li_2O{\cdot}2SiO_2$ single crystal, obtained by X-ray diffraction technique, are also shown in Fig. 14. The expansions of all of the ingots in the direction parallel to their solidification directions were linear up to 900°C as shown in Fig. 14(A), and their expansion

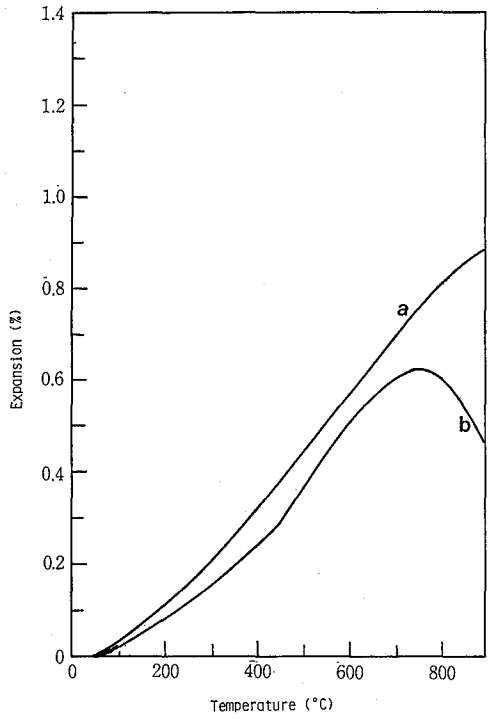

Fig. 13. Thermal expansions of the $100(Li_2O \cdot 2SiO_2)3B_2O_3$ ingot in the directions parallel (a) and perpendicular (b) to its solidification direction.

coefficients were almost identical to that of the *c*-axis of the $Li_2O \cdot 2SiO_2$ single crystal, *i.e.*$\sim 140 \times 10^{-7}$/°C, irrespective of their solidification rates and compositions.

The expansions of the ingots in the direction perpendicular to their solidification directions, however, depended on their solidification rates and compositions as shown in Fig. 14(B); *i.e.* the thermal expansion coefficients in the temperature range 300 to 700°C varied wide from 100 to 145×10^{-7}/°C and the thermal expansions of some ingots showed a sharp bend at 700°C to 800°. The dependence of the thermal expansion on the solidification rates and compositions of the ingots can be explained in terms of the presence of the glassy phase and crystalline phases other than the $Li_2O \cdot 2SiO_2$ crystal, the kind and the amount of which are strongly affected by the solidification rates and compositions of the ingots, at the boundaries of the columnar $Li_2O \cdot 2SiO_2$ crystals.

7. Sound Velocity in the Ingot

The propagation rates of the 12 MHz longitudinal sound wave in the ingots given in Table I were generally high and almost constant, 7.10–7.30 Km/s, in the direction parallel to the solidification directions of the ingots, whereas in the direction perpendicular to their solidification directions they were generally low and varied markedly from 1.20 to 6.20 Km/s depending on their solidification rates and compositions. The plots of the propagation rates in the ingots against their porosities (Fig. 15) indicated that the propagation rates are independent of the porosities in the direction parallel to the solidification directions of the ingots, whereas they, in the direction perpendicular to their solidification directions, decrease markedly with increasing porosity.

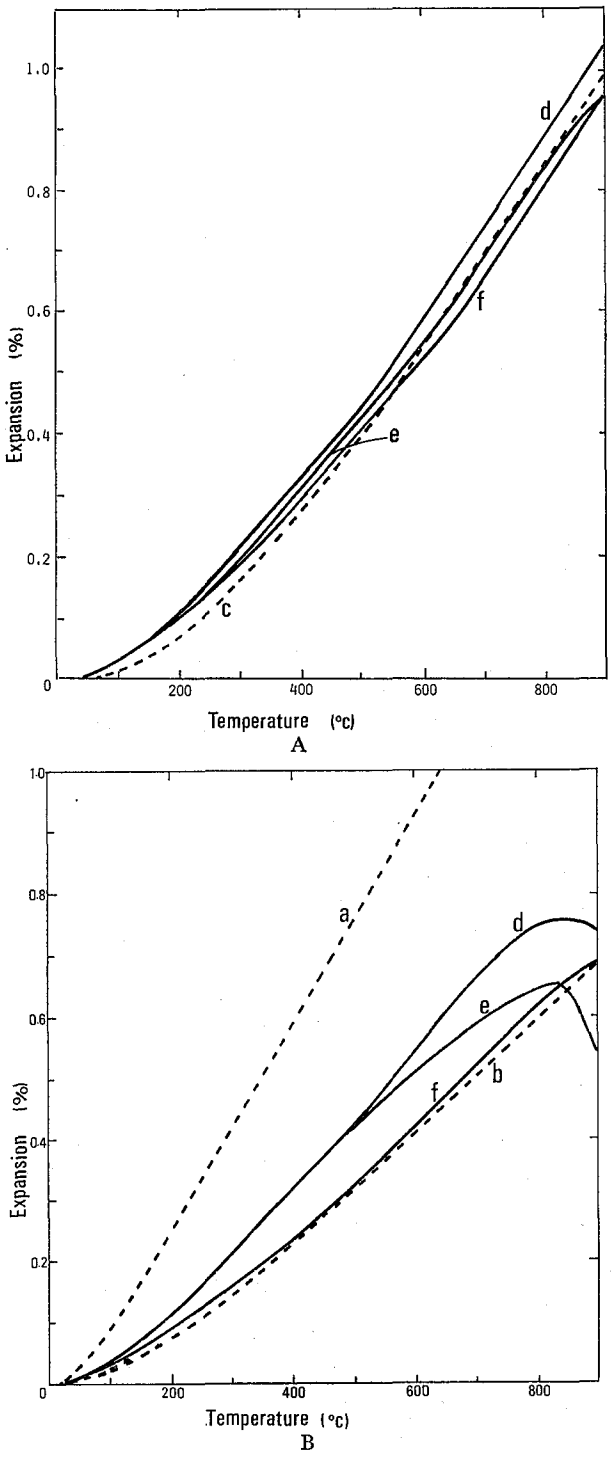

Fig. 14. Thermal expansions of the $Li_2O{\cdot}2SiO_2$ (d), $100(Li_2O{\cdot}2SiO_2)3Na_2O$ (e) and $100(Li_2O{\cdot}2SiO_2)3Al_2O_3$ (f) ingots all solidified at a rate of 1.3 mm/h, in the directions parallel (A) and perpendicular (B) to the solidification direction, respectively. a, b, and c; Thermal expansions of $Li_2O{\cdot}2SiO_2$ single crystal in its *a*-, *b*- and *c*-axes.

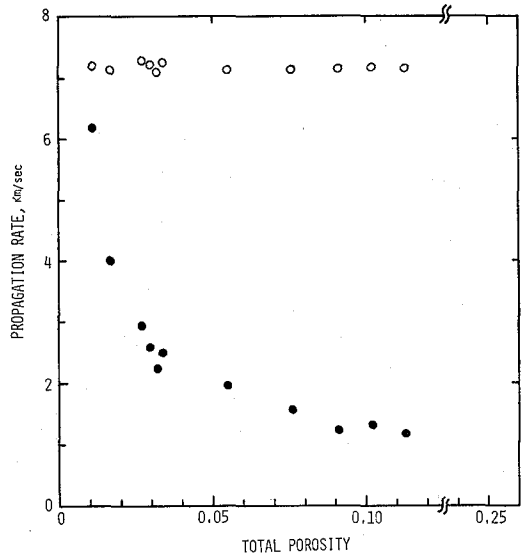

Fig. 15. Propagation rates of 12 MHz longitudinal sound wave in the ingots in the directions parallel (○) and perpendicular (●) to their solidification directions as a function of their porosities.

These results can be explained in terms of the presence of the openings such as the cylindrical pores or microcracks at the boundaries between the columnar $Li_2O \cdot 2SiO_2$ crystals oriented with their *c*-axes parallel to the solidification directions of the ingots.

8. Compressive Strength of the Ingot

The compressive strengths of the ingots were generally high and almost constant, 2300 to 2700 Kg/cm², in the direction parallel to their solidification directions, except for those of a few ingots having porosities higher than about 7%. On the other hand, the compressive strengths of the ingots (*S*) in the direction perpendicular to their solidifi-

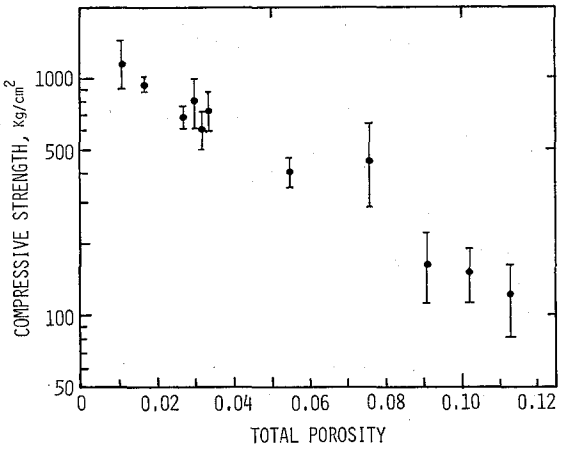

Fig. 16. Compressive strengths of the ingots in the direction perpendicular to their solidification directions as a function of their porosities.

cation directions were generally low and decreased markedly from 1170 to 120 Kg/cm^2 with increasing porosity (p), as shown in Fig. 16. The relation between S and p was expressed by;

$$S \propto \exp(-25p) \tag{13}$$

These results can be explained on the basis of the assumption of Knudsen[51] that the change in strength which accompanies a change in specimen porosity is attributable to an associate change in the size of the critical loadbearing area within the specimen. For the ingots with the microstructure described in the preceding section, the critical area bearing loads in the direction parallel to the solidification direction of the ingots is probably proportional to $(1-p)$, where p is the porosity of the ingots, and, therefore, the compressive strength of the ingots will be proportional to $(1-p)$. For the small values of p, the change in compressive strength with porosity will be negligibly small as verified experimentally.

Estimation of the critical area (A) bearing loads in the direction perpendicular to the solidification directions of the ingots is somewhat complex, but it can be expressed by;

$$A \propto \exp(-27p) \tag{14}$$

This relation applies within the range of $p=0$ to 7%. The theoretical method of derivation of this relation was reported in detail elsewhere[40]; in principle, it is based on the assumption that the columnar crystals with the same diameter are aligned in closest packing and their contact is represented simply as flat junction between the columnar crystals partially planed with their surfaces. According to the relation (14), the critical area in the ingots bearing the loads perpendicular to their solidification directions will change markedly with their porosities, and, consequently, the compressive strength of the ingots in the direction perpendicular to their solidification directions will also change markedly with their porosities, as found experimentally.

IV. SUMMARY

The melts with the compositions of $Li_2O{\cdot}2SiO_2$ and $100(Li_2O{\cdot}2SiO_2)3R_mO_n$, where R_mO_n is Na_2O, MgO, B_2O_3, Al_2O_3, SiO_2 or P_2O_5, were unidirectionally solidified in clay crucibles at various rates ranging from 0.7 to 13 mm/h under a constant temperature gradient of 80°C/cm. The relations between the microstructures of the ingots and their solidification conditions as well as those between their physical properties and microstructures were investigated. The results are summarized as follows.

1. All the ingots were composed of primarily $Li_2O{\cdot}2SiO_2$ columnar crystals and a small amount of glassy phase. Some other minor crystalline phases were existent in the $100(Li_2O{\cdot}2SiO_2)3R_mO_n$ ingots.

2. The $Li_2O{\cdot}2SiO_2$ columnar crystals did not show preferred orientation in the ingots when the melts were solidified in an as-prepared clay crucible with a fresh bottom surface, whereas they were well aligned with their c-axes parallel to the solidification direction of the ingots when the melts were solidified in the clay crucible, the bottom of which was covered with a $Li_2O{\cdot}2SiO_2$ glass-ceramic layer.

3. The mean diameter of the $Li_2O \cdot 2SiO_2$ columnar crystals (D) in the $Li_2O \cdot 2SiO_2$ ingots decreased from 580 to 340 μm with increasing solidification rate (R) according to the relation, $D \propto R^{-1/6}$. It also decreased markedly with addition of the third components such as MgO and Al_2O_3.

4. Many cylindrical pores were found in the $Li_2O \cdot 2SiO_2$ ingots solidified at rates higher than 3.3 mm/h and also in the $100(Li_2O \cdot 2SiO_2)3Al_2O_3$(or P_2O_5) ingots solidified even at a rate of 1.3 mm/h. The porosities of their ingots exceeded 5%. No cylindrical pores were found in all of the other ingots solidified at a rate of 1.3 mm/h, but microcracks were found at the boundaries of the columnar $Li_2O \cdot 2SiO_2$ crystals. Their porosities ranged from 1.1 to 3.4%.

5. The cylindrical pores were probably formed during the solidification of the melts by the process in which the H_2O originally dissolved in the melts first accumulated at the crystal-melt interface, then formed bubbles in the melts and was finally caught by the growing crystals. Change in the H_2O concentration distribution in the melt with time during its solidification, the critical supersaturated concentration of the H_2O in the melt at which the H_2O gas bubbles start to form, and the rising rate of the bubbles in the melt were estimated quantitatively.

6. The microcracks were probably formed by the thermal stresses, which were induced by a large difference in the thermal expansions between a- and b-axes of the unidirectionally oriented columnar $Li_2O \cdot 2SiO_2$ crystals, during cooling of the ingots from their solidification temperature to room temperature. The porosities of the ingots due to the existence of the microcracks, which were in the range below about 4%, decreased with increasing glass content of the ingots. The glassy phase probably suppressed the formation of the microcracks by its viscous flow. The addition of the Na_2O or B_2O_3 was effective in increasing the amount of the glassy phase in the ingots.

7. The thermal expansion coefficient, propagation rate of sound wave and compressive strength of the ingots, all in the direction parallel to the solidification direction of the ingots, were almost independent of the solidification rates and compositions of the ingots, whereas they, in the direction perpendicular to the solidification direction, varied markedly depending on the solidification rates and the compositions. These anisotropic properties of the ingots were explained in terms of the presence of the openings such as the cylindrical pores or microcracks and also of a small amount of the glassy phase and crystalline phases other than the $Li_2O \cdot 2SiO_2$ crystal all at the boundaries between the columnar $Li_2O \cdot 2SiO_2$ crystals well oriented with their c-axes parallel to the solidification direction of the ingots.

APPENDIX

Kracek[41] reported in his paper on the phase equilibrium in the system Li_2O-SiO_2, that "the disilicate disappears at 1033°, leaving very rare Li_2SiO_3 and liquid. The Li_2SiO_3 disappears from this preparation just below 1035°. The order of uncertainty in these determinations is very near the limit of experimental precision; the most probable interpretation is that $Li_2Si_2O_5$ just misses having a stable melting point".

According to his experimental results, one has to conclude theoretically that $Li_2O \cdot 2SiO_2$ melts incongruently.

Practically, however, $Li_2O \cdot 2SiO_2$ can be treated as the congruent melting composition, especially in the process of solidification of the $Li_2O \cdot 2SiO_2$ melt, since the range of its incongruently melting temperature is only 1035°–1033°C=2°C, as Kracek reported. The present authors confirmed that no $Li_2O \cdot SiO_2$ crystal precipitated in the melt in the process of solidification of the $Li_2O \cdot 2SiO_2$ melt; the $Li_2O \cdot 2SiO_2$ crystal precipitated directly from the melt.

REFERENCES

(1) T. Takada, Y. Ikeda, H. Yoshinaga, and Y. Bando, Proc. Inter. Conf. Ferrite, 1970, p. 275.
(2) M. H. Hodge, W. R. Bitler, and R. C. Bradt, *J. Am. Ceram. Soc.*, **56**, 497 (1973).
(3) T. Nishikawa, T. Nishida, K. Inoue, H. Inoue, and I. Uei, *Yogyo-Kyokai-Shi*, **82**, 241 (1974).
(4) K. Kugimiya, E. Hirota, and Y. Bando, *IEEE Trans. Mag.*, **MAG-10** (3) 907 (1974).
(5) T. Nishikawa, T. Nishida, and S. Sugimura, *Yogyo-Kyokai-Shi*, **83**, 110 (1975).
(6) T. Nishikawa, T. Nishida, and T. Uno, *ibid.*, **85**, 354 (1977).
(7) F. M. A. Carpay and W. A. Cense, *Nature Phys. Sci.*, **241**, 19 (1973).
(8) F. M. A. Carpay and W. A. Cense, *Scripta Met.*, **8**, 11 (1974).
(9) F. M. A. Carpay and W. A. Cense, *J. Cryst. Growth*, **24/25**, 551 (1974).
(10) K. H. G. Ashbee, *Nature*, **252**, 469 (1974).
(11) K. H. G. Ashbee, *J. Mater. Sci.*, **10**, 911 (1975).
(12) D. I. H. Atkinson and P. W. McMillan, *ibid*, **10**, 2012 (1975).
(13) D. I. H. Atkinson and P. W. McMillan, *ibid*, **12**, 443 (1977).
(14) A. Maries and P. S. Rogers, *J. Mater. Sci.*, **13**, 2119 (1978).
(15) R. M. Weston and P. S. Rogers, *Mineral. Mag,*. **42**, 325 (1978).
(16) P. S. Rogers and R. M. Weston, *J. Mater. Sci.*, **14**, 1192 (1979).
(17) F. S. Galasso, W. L. Parly, F. C. Douglas, and J. A. Batt, *J. Am. Ceram. Soc.*, **50**, 333 (1967).
(18) D. E. Harrison, *J. Cryst. Growth*, **3**, **4**, 674 (1968).
(19) D. Viechnicki and F. Schmid, *J. Mater. Sci.*, **4**, 84 (1969).
(20) D. J. Rowcliffe, W. J. Warren, A. G. Elliot, and W. S. Rothwell, *J. Mater. Sci.*, **4**, 902 (1969).
(21) F. Schmid and D. Viechnicki, *ibid,*. **5**, 470 (1970).
(22) F. Schmid and D. Viechnicki, "Advanced Materials, Composites and Carbon", Am. Ceram. Soc., Inc., Ohio, 1971, p. 96.
(23) C. O. Hulse and J. A. Batt, *ibid.*, p. 132.
(24) G. Dhalenne, A. Revcolevschi, and R. Collongues, *Mater. Res. Bull.*, **7**, 1385 (1972).
(25) F. L. Kennard, R. C. Bradt, and V. S. Stubican, in "Reactivity of Solids", J. S. Anderson *et al.* Ed., Chapman and Hall, London, 1972, p. 580.
(26) F. L. Kennard, R. C. Bradt, and V. S. Stubican, *J. Am. Ceram. Soc.*, **56**, 566 (1973).
(27) F. L. Kennard, R. C. Bradt, and V. S. Stubican, *ibid.*, **57**, 428 (1974).
(28) C. Hulse and J. Batt, United Aircraft Research Laboratories Report N910803-10, 1974.
(29) J. Van Den Boomgaard, D. R. Terrell, R. A. J. Born, and M. F. J. I. Gill, *J. Mater. Sci.*, **9**, 1705 (1974).
(30) A. M. J. G. Van Run, D. R. Terrell, and J. H. Scholig, *ibid.*, **9**, 1710 (1974).
(31) F. L. Kennard, R. C. Bradt, and V. S. Stubican, *J. Am. Ceram. Soc.*, **59**, 160 (1976).
(32) K. P. Gupta, in "Treatise on Materials Science and Technology", Vol. 9, F. F. Wang Ed., Academic Press, New York, 1976, p. 305.
(33) R. L. Ashbrook, *J. Am. Ceram. Soc.*, **60**, 428 (1977).
(34) W. E. Kramer, R. H. Hopkins, and M. R. Daniel, *J. Mater. Sci.*, **12**, 409 (1977).
(35) W. J. Minford, R. C. Bradt, and V. S. Stubican, *J. Am. Ceram. Soc.*, **62**, 154 (1979).
(36) M. Arioka, T. Kokubo, and M. Tashiro, *Yogyo-Kyokai-Shi.* **85**, 501 (1977).
(37) M. Arioka, T. Kokubo, and M. Tashiro, *ibid.*, **86**, 368 (1978).
(38) M. Arioka, T. Kokubo, and M. Tashiro, *ibid.*, **86**, 512 (1978).
(39) M. Arioka, T. Kokubo, and M. Tashiro, *J. Chem. Soc., Japan, Chem. Ind. Chem.*, 1357 (1978).
(40) M. Arioka, T. Kokubo, and M. Tashiro, *Yogyo-Kyokai-Shi*, **87**, 182 (1979).
(41) F. C. Kracek, *J. Phys. Chem.*, **34**, 2642 (1930).

(42) S. M. Ohlberg and D. W. Strickler, *J. Am. Ceram. Soc.*, **45**, 170 (1962).
(43) F. K. Lotgering, *J. Inorg. Nucl. Chem.*, **9**, 113 (1959).
(44) F. Liebau, *Acta Cryst.*, **14**, 389 (1961).
(45) E. Schreiber, O. L. Anderson, and N. Soga, "Elastic Constant and Their Measurement", McGraw-Hill, 1973, p. 35.
(46) H. Scholze, *Glass Ind.*, **47**, 546, 622 and 670 (1966).
(47) H. Scholze, *Glastech. Ber.*, **32**, 81 (1959).
(48) M. Cable, *J. Am. Ceram. Soc.*, **49**, 436 (1966).
(49) L. Shartsis, S. Spinner, and W. Capps, *J. Am. Ceram. Soc.*, **35**, 155 (1952).
(50) H. Scholze and H. Mulfinger, *Glastech. Ber.*, **32**, 381 (1959).
(51) F. P. Knudsen, *J. Am. Ceram. Soc.*, **42**, 376 (1959).